

Enhanced Thermoelectric Performance of p -type BiSbTe Through Incorporation of Magnetic CrSb

Raphael Fortulan^{1,2}, Suwei Li,³ Michael John Reece,³ Illia Serhiienko,^{4,5} Takao Mori,^{4,5} and Sima Aminorroya Yamini⁶

¹*Materials and Engineering Research Institute, Sheffield Hallam University, Sheffield, UK*

²*Present address: Unconventional Computing Laboratory, University of the West of England, Bristol, UK*

³*School of Engineering and Material Science, Queen Mary University of London, Mile End Road, London E1 4NS, UK*

⁴*International Center for Materials Nanoarchitectonics (WPI-MANA), National Institute for Materials Science, Tsukuba, Japan*

⁵*Graduate School of Pure and Applied Science, University of Tsukuba, Tsukuba, Japan*

⁶*School of Aerospace, Mechanical and Mechatronic Engineering, The University of Sydney, Sydney, 2006, Australia*

(*Electronic mail: raphael.vicentefortulan@uwe.ac.uk)

There is evidence that magnetism can potentially increase the thermopower of materials, most likely due to magnon scattering, suggesting the incorporation of intrinsic magnetic semiconductors in non-magnetic thermoelectric materials. Here, samples of p -type $\text{Bi}_{0.5}\text{Sb}_{1.5}\text{Te}_3$ with 10 at.% excess Te are ball-milled with varying ratio of the antiferromagnetic semiconductor CrSb (0, 0.125, 0.5, and 1 wt.%) to prepare bulk samples by spark plasma sintering technique. The thermopower of samples containing CrSb is increased due to an increase in the effective mass of the charge carriers, indicating that there is a drag effect originating from the magnetic particles. However, this was at the expense of reduced electrical conductivity caused by reduced charge carrier mobility. While overall only marginal improvements in power factors were observed, these samples exhibited significantly lower thermal conductivity compared to the single-phase material. As a result, a peak zT value of ~ 1.4 was achieved at 325 K for the sample with 0.125 wt.% CrSb. These results highlight the potential of incorporating magnetic secondary phases to enhance the

thermoelectric performance of materials.

INTRODUCTION

To create a high-performance thermoelectric material, one must simultaneously achieve a high power factor ($PF = \alpha^2 \sigma$) and a low total thermal conductivity (κ). However, α , σ , and κ exhibit strong correlations¹⁻³, making the task of optimizing one parameter independently, while keeping the others constant, extremely challenging.

Bismuth telluride alloys are among the most efficient thermoelectric materials for near-room-temperature applications. Alloying Bi_2Te_3 with Sb_2Te_3 optimizes parameters such as carrier concentration, lattice thermal conductivity, and electronic band structure to improve the figure of merit $zT = PF/\kappa T$ ^{4,5}. However, the thermoelectric performance of these alloys is limited by their relatively low thermopower.

The use of magnetism has emerged as a promising strategy to increase thermopower through mechanisms such as paramagnon drag and spin-dependent effects⁶⁻⁹. The concept that magnetism can possibly enhance thermoelectric properties dates back decades, with early work proposing that magnon scattering could be the origin of an increase in the thermopower of some magnetic elements at low temperatures¹⁰. These include (1) using intrinsically magnetic semiconductors, such as MnTe ¹¹, CuFeS_2 ^{12,13}, and $\text{Cr}_2\text{Ge}_2\text{Te}_6$ ¹⁴; (2) doping non-magnetic thermo-

electric materials with magnetic elements resulting in increased thermopower due to interactions between charge carriers and local magnetic moments^{6,15-18}; and (3) introducing magnetic secondary phases, such as nanoparticles or inclusions, into non-magnetic thermoelectric matrices¹⁹⁻²². Studies on $\text{Ba}_{0.3}\text{In}_{0.3}\text{Co}_4\text{Sb}_{12}$ ^{19,23} and $\text{Ti}_{0.25}\text{Zr}_{0.25}\text{Hf}_{0.5}\text{NiSnSb}$ ²⁰ materials have shown that the inclusion of coherent magnetic particles can simultaneously enhance thermopower and carrier mobility. Magnetic secondary phases may allow the tuning of properties through the composition, size, and microstructure of the materials²⁴⁻²⁸.

In this study, ball-milled stoichiometric $\text{Bi}_{0.5}\text{Sb}_{1.5}\text{Te}_3$ 10 at.% Te-rich and CrSb (0, 0.125, 0.5, and 1 wt.%) samples were fabricated by spark plasma sintering (SPS). Excess Te was added to the system as Te-rich bismuth telluride and bismuth antimony telluride alloys showed high thermoelectric performance²⁹⁻³². The inclusion of excess Te suppresses the defects caused by its easy volatilization during the SPS process³³ and this strategy has been shown to result in more efficient thermoelectric materials³². CrSb is an antiferromagnetic semiconductor with a Néel temperature of approximately 680 K³⁴, which makes it a promising magnetic secondary phase candidate for improving the thermoelectric performance for room temperature applications.

By incorporating varying concentrations of magnetic CrSb particles, we were able to increase the thermopower through indicated drag effect, while maintaining a relatively high electrical conductivity. The addition of a secondary phase introduces additional phonon scattering mechanisms that reduce thermal conductivity. This reduction combined with a higher thermopower, enabled a high peak of $zT \approx 1.4$ at 325 K.

EXPERIMENTAL DETAILS

Synthesis

Polycrystalline $\text{Bi}_{0.5}\text{Sb}_{1.5}\text{Te}_{3+0.3}$ samples were synthesized by direct reaction of stoichiometric amounts of Bi (99.999%, Alfa Aesar), Te (99.999%, Alfa Aesar), and Sb (99.999%, Alfa Aesar) in vacuum-sealed quartz ampules in an inert atmosphere glovebox. The ampules were heated to 850 °C for 12 h, homogenized at 1000 °C, quenched in cold water, and annealed at 400 °C for 72 h.

A pristine CrSb sample was synthesized by loading stoichiometric amounts of Cr (99.95%, Alfa Aesar) and Sb (99.999%, Alfa Aesar) into a vacuum-sealed quartz ampule. The ampule was heated to 850 °C for 24 h, mixed every 4 h, homogenized at 1160 °C for 1 h, and allowed to cool naturally. The resulting ingot was hand-ground using an agate mortar and pestle in a glovebox, loaded into a vacuum-sealed quartz

ampule, and annealed at 900 °C for 24 h. The annealed powder was then sintered in a graphite die under vacuum to make \varnothing 11 mm rods using SPS (KCE FCT-H HP D-25 SD, FCT Systeme GmbH, Rauenstein, Germany) at 50 MPa for 20 min at 900 °C.

Samples of $\text{Bi}_{0.5}\text{Sb}_{1.5}\text{Te}_3$ with x wt.% CrSb ($x = 0, 0.125, 0.5, \text{ and } 1$) were fabricated by wet ball milling powdered ingots of $\text{Bi}_{0.5}\text{Sb}_{1.5}\text{Te}_{3+0.3}$ and CrSb. The cast ingots were pre-milled using an agate mortar and pestle in a glovebox. The powders were weighed and placed in a 250 mL agate jar with 20 mm agate balls and ethanol (99.97%, VWR). The ball-to-powder ratio was 15:1, and the solvent-to-powder ratio was 100 mL to 10 g³⁵. Milling was performed using a Retsch Planetary Ball Mill PM 100 at 300 rpm for 4 h at 15 min intervals with 5 min breaks and a change in direction halfway through. The jar was then placed in a desiccator for at least 15 h. The dried powders were sintered in a graphite die under vacuum to make \varnothing 11 mm rods using SPS at 50 MPa for 5 min at 400 °C. The densities of all samples were approximately 95% of their nominal density.

Materials characterization

The phase purity and crystal structure of the sintered samples were characterized by Powder X-ray Diffraction (PXRD) using a PANalytical X'Pert Pro diffractometer with $\text{CuK}\alpha 1$ radiation

($\lambda = 0.15406$ nm, 40 kV, 40 mA).

Electrical conductivity (σ) and thermopower (α) were measured perpendicular to the sintering direction of the samples by cutting $\approx 2 \times 2 \times 8$ mm³ bar specimens from the rods. Measurements were conducted from room temperature to 523 K under a helium atmosphere using a Linseis LSR-3 apparatus.

The thermal diffusivity (D) of all the samples was measured by the LFA method using a NETZSCH LFA 467 HyperFlash[®] instrument. Slab-shaped samples were also cut to measure the room-temperature Hall coefficient (R_H) under a ± 0.55 T magnetic field using an ECOPIA 3000 Hall Effect Measurement System. The Hall carrier concentration (n_H) was calculated as $n_H = 1/(e \cdot R_H)$.

Heat capacity measurements were conducted from room temperature to 473 K using a PerkinElmer DSC 8000 according to the ASTM sapphire standard method E1269³⁶. The measured heat capacity values are presented in the Appendix A.

RESULTS AND DISCUSSION

Structural and phase analysis

The PXRD patterns of all samples in Fig. 1 match the rhombohedral $\text{Bi}_{0.5}\text{Sb}_{1.5}\text{Te}_3$ phase. The inset shows that the diffraction pattern of the pristine CrSb sample corresponds to a single-

phase CrSb hexagonal structure.

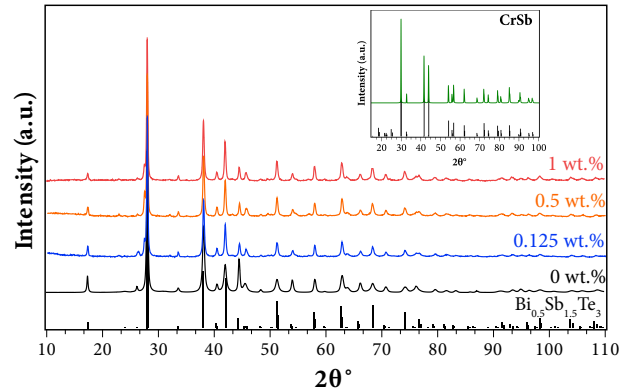


FIG. 1. Powder X-ray diffraction patterns of $\text{Bi}_{0.5}\text{Sb}_{1.5}\text{Te}_{3+0.3}$ with x wt.% CrSb ($x = 0, 0.125, 0.5,$ and 1) samples. The inset shows the diffraction pattern for pristine CrSb.

Transport properties

Figs. 2(a) to (c) show the thermopower, electrical conductivity, and power factor of $\text{Bi}_{0.5}\text{Sb}_{1.5}\text{Te}_{3+0.3}$ with x wt.% CrSb ($x = 0, 0.125, 0.5,$ and 1), measured perpendicular to the direction of sintering. All samples showed a positive thermopower (Fig. 2(a)), indicating p -type semiconductor behavior. The electrical conductivity exhibited metallic behavior with decreasing values, as seen in Fig. 2(b).

The room-temperature values of the thermopower increase with the concentration of the CrSb, rising from $\sim 238 \mu\text{V}\cdot\text{K}^{-1}$ for the single-phase sample to $\sim 280 \mu\text{V}\cdot\text{K}^{-1}$ for the 1 wt.% CrSb. With the opposite effect on electrical conductivity, the electrical conductivity of the single-

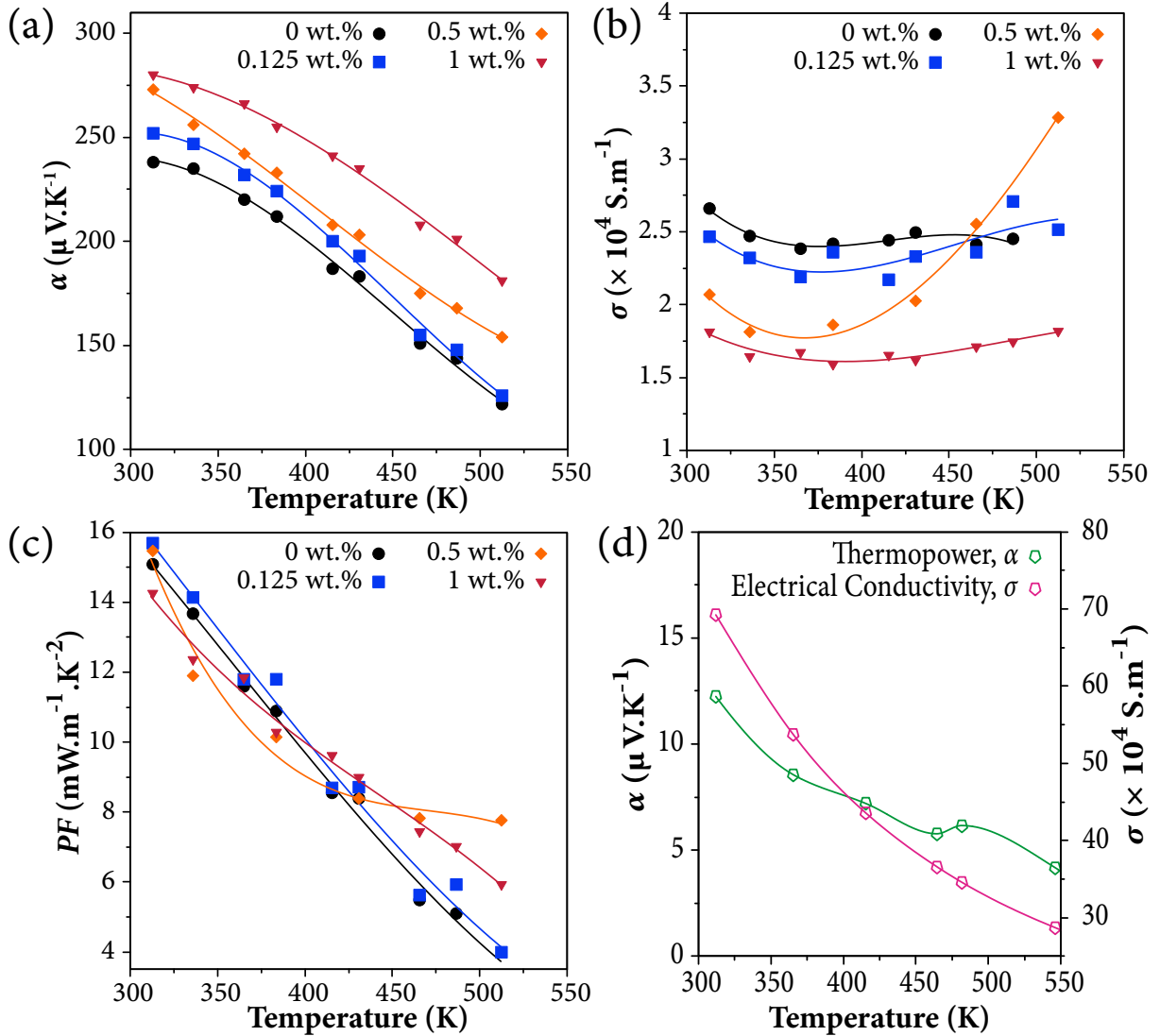


FIG. 2. Temperature dependence of the (a) thermopower, (b) electrical conductivity, and (c) power factor of Bi_{0.5}Sb_{1.5}Te_{3+0.3} with x wt.% CrSb ($x = 0, 0.125, 0.5, \text{ and } 1$) samples, and (d) thermopower and electrical conductivity of pristine CrSb.

phase sample decreased from $\sim 2.7 \times 10^4 \text{ S}\cdot\text{m}^{-1}$ for the single-phase sample to $\sim 1.8 \times 10^4 \text{ S}\cdot\text{m}^{-1}$ for the sample with 1 wt.% CrSb. thermopower are comparable to the one seen in the literature³⁷.

Fig. 2(d) shows the temperature-dependent electrical transport properties of pristine CrSb samples measured perpendicularly to the sintering direction. The electrical conductivity and

Table I lists the Hall carrier concentrations and mobilities of the samples. The carrier concentration of these samples is lower than those observed in the literature ($\sim 1 \times 10^{19} \text{ cm}^{-3}$) which results in the overall lower electrical con-

ductivity of these samples. The mobility of 232 $\text{cm}^2.\text{V}^{-1}.\text{s}^{-1}$ for the single-phase samples is similar to those reported in the literature (e.g., 248 $\text{cm}^2.\text{V}^{-1}.\text{s}^{-1}$ ²⁹). The values of n_{H} ranged from $7.7 \sim 7.1 \cdot 10^{18} \text{ cm}^{-3}$, indicating that the excess Te stabilized the carrier concentration of the samples. However, the mobility decreases with the inclusion of the secondary phase, which is consistent with the behavior of multiphase materials^{38,39}.

TABLE I. Room temperature Hall carrier concentration and mobility of ball milled $\text{Bi}_{0.5}\text{Sb}_{1.5}\text{Te}_{3+0.3}$ with x wt.% CrSb ($x = 0, 0.125, 0.5,$ and 1) samples

x	$n_{\text{H}} (\times 10^{18} \text{ cm}^{-3})$	$\mu_{\text{H}} (\text{cm}^2.\text{V}^{-1}.\text{s}^{-1})$
0	7.7	232.0
0.125	7.7	203.9
0.5	7.3	185.5
1	7.1	161.6

Since the carrier concentration of all samples has similar values, these changes cannot simply be attributed to changes in the values of n_{H} . The behavior of the band structure with CrSb inclusion was analyzed by modeling the thermopower and Hall carrier concentration using the single parabolic band (SPB) model⁴⁰ (discussed in the Appendix B). The SPB model used here may not fully and accurately determine the behavior of multiphase samples due to the presence of bipolar conduction, complex scattering processes, and the non-parabolic nature of the

valence band. However, this approach may indicate a trend in the calculated effective mass, m^* , of samples⁴¹.

TABLE II. Calculated effective mass of ball milled $\text{Bi}_{0.5}\text{Sb}_{1.5}\text{Te}_{3+0.3}$ with x wt.% CrSb ($x = 0, 0.125, 0.5,$ and 1) samples using the single parabolic band model

x	$m^*(m_0)$
0	0.90
0.125	1.16
0.5	1.06
1	1.21

The effective mass of samples is increased in the presence of CrSb Table II. Since the thermopower for a degenerate semiconductor, with a parabolic band and energy-independent scattering approximation, can be written as⁴⁰

$$\alpha = \frac{8\pi^2 k_{\text{B}}}{3qh^2} m^* T \left(\frac{\pi}{3n} \right)^{2/3}, \quad (1)$$

where m^* is the effective mass, Eq. (1) suggests that the presence of a magnetic phase in the material can lead to an increase in the effective mass of the sample and consequently an increase in the thermopower, similar to observations of studies with magnetic dopants^{15,42}.

The results show that despite the presence of a magnetic secondary phase with poor thermoelectric performance and low thermopower of approximately $12.5 \mu\text{V}.\text{K}^{-1}$ at room temperature and $4.38 \mu\text{V}.\text{K}^{-1}$ at 550 K, the electronic performance of the samples can be improved rather

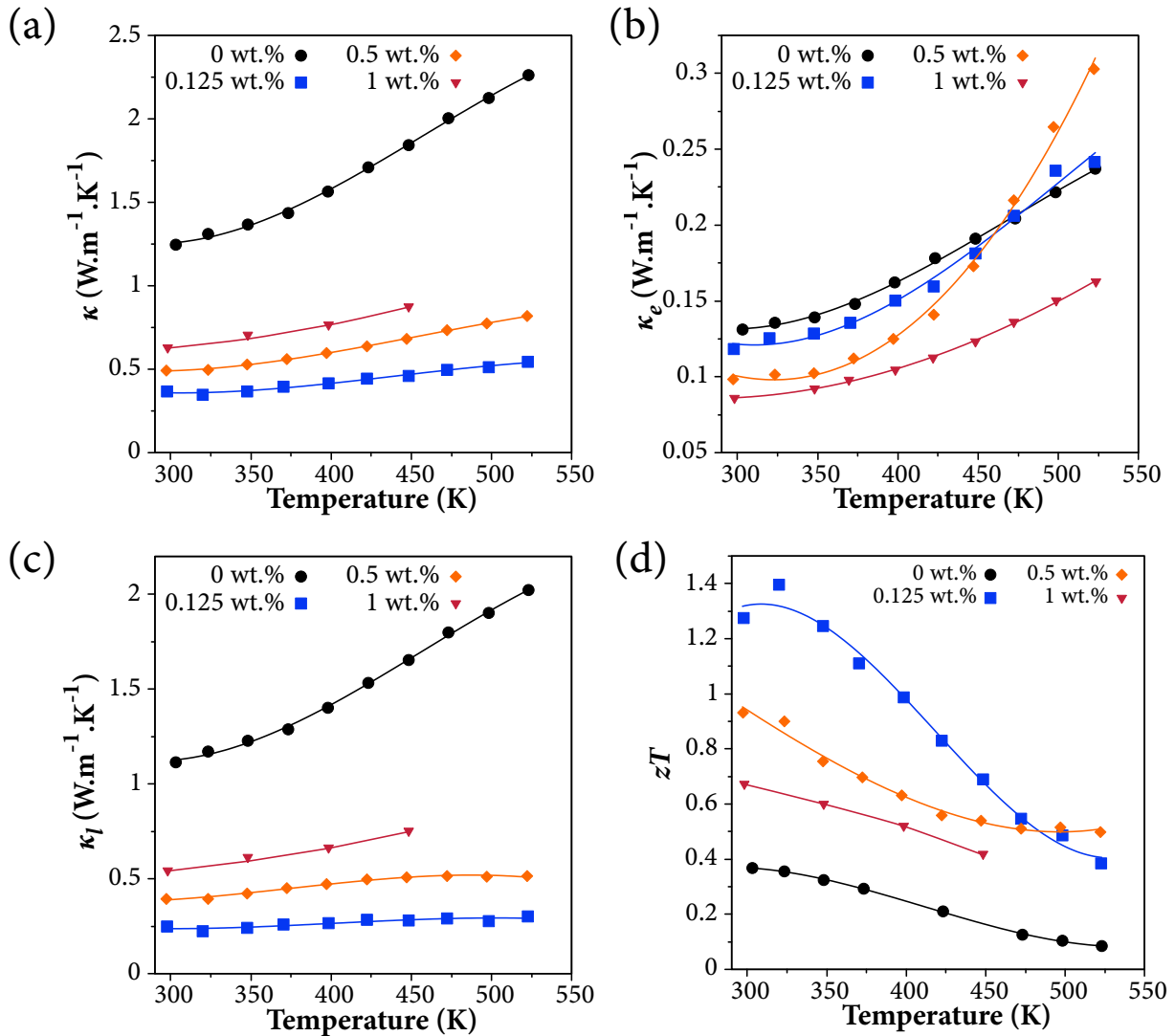


FIG. 3. Temperature dependence of the (a) thermal conductivity, (b) electronic thermal conductivity, (c) lattice thermal conductivity, (d) figure of merit zT of Bi_{0.5}Sb_{1.5}Te_{3+0.3} with x wt.% CrSb ($x = 0, 0.125, 0.5,$ and 1) samples.

than degraded (see Fig. 2(d)).

The combined decrease in carrier mobility due to the presence of an additional phase and the possible dragging effect caused by the magnetic phase degrade the electrical conductivity of multiphase samples¹⁵. However, the overall effect, was an increase in the power factor PF

was detected (as shown in Fig. 2(c)).

The thermal conductivity (κ) of the samples is shown in Fig. 3(a). The electronic contribution to the thermal conductivity (κ_e) is shown in Fig. 3(b) and it was estimated using the Wiedemann-Franz law⁴³ ($\kappa_e = L\sigma T$) where L is the Lorenz number, and it was calculated us-

ing the SPB model (see Appendix B for more details).

The lattice (κ_l) contributions to thermal conductivity were calculated as $\kappa_l = \kappa - \kappa_e$, as shown in Fig. 3(c). The measured values for the lattice thermal conductivity are optimally low reaching values slightly below the glass-like thermal conductivity for Bi_2Te_3 ($\kappa_{\text{glass}} \approx 0.31 \text{ W.m}^{-1}.\text{K}^{-130}$) but higher than Cl-doped Bi_2Te_3 alloys ($0.15 \text{ W.m}^{-1}.\text{K}^{-144}$), namely the sample containing the 0.125 wt.% of CrSb reached the lowest value of $\sim 0.24 \text{ W.m}^{-1}.\text{K}^{-1}$. The low values for all samples indicate a high degree of scattering of the phonons due to additional boundaries introduced by the secondary phase.

The figure of merit (zT) of the samples is shown in Fig. 3(d). The combination of significantly reduced thermal conductivity, aligned with an increase in thermal power due to the incorporation of the magnetic secondary phase, contributed to the high zT values for the multiphase samples compared to the single-phase $\text{Bi}_{0.5}\text{Sb}_{1.5}\text{Te}_{3+0.3}$ material. We note that our single-phase sample has a relatively low zT value of around 0.36, similar to what was observed for⁴⁵, and indicate the maximum zT for this sample was below room temperature⁴⁶.

The 0.125 wt.% CrSb sample exhibited the highest zT , reaching a peak value of ~ 1.4 at 325 K. The other multiphase compositions also showed promising zT improvements, albeit to

a lesser extent. The 0.5 wt.% CrSb had the next highest zT of ~ 0.92 at 525 K, followed by the 1 wt.% CrSb at ~ 0.68 . The high zT values result from the synergistic effects of magnetically induced thermopower enhancement and thermal conductivity reduction due to interfacial and magnetic scattering in the multiphase samples.

In Fig. 4, the results obtained in this work are compared with other compositions seen in the literature⁴⁷⁻⁵², as well as with a commercial BiSbTe ingot. The introduction of the CrSb phase in the $\text{Bi}_{0.5}\text{Sb}_{1.5}\text{Te}_{3+0.3}$ material shows a performance that surpasses the one seen for the commercial ingot and is comparable to the best results reported in the literature for composite BiSbTe materials.

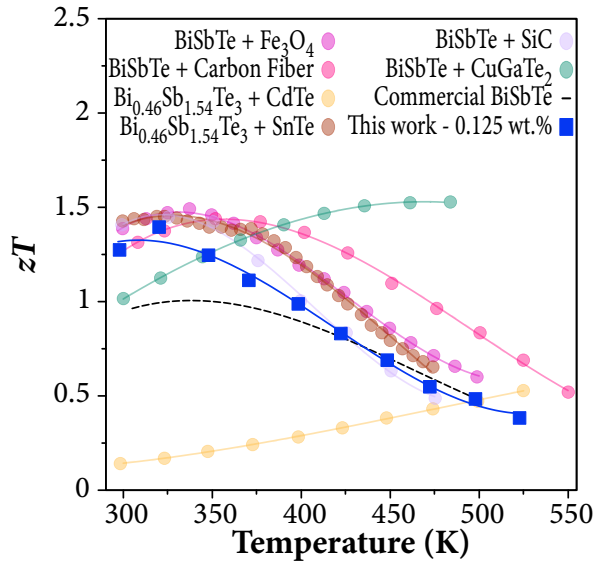


FIG. 4. Temperature dependence of zT of $\text{Bi}_{0.5}\text{Sb}_{1.5}\text{Te}_{3+0.3}$ with x wt.% CrSb ($x = 0, 0.125, 0.5,$ and 1) samples. Comparisons of zT values of $\text{Bi}_{0.5}\text{Sb}_{1.5}\text{Te}_{3+0.3} + 0.125$ wt.%, commercial BiSbTe, and other typical p -type BiSbTe composites: $\text{Bi}_{0.5}\text{Sb}_{1.5}\text{Te}_3 + \text{Fe}_3\text{O}_4$ ⁴⁷, $\text{Bi}_{0.5}\text{Sb}_{1.5}\text{Te}_3 + \text{carbon fiber}$ ⁴⁸, $\text{Bi}_{0.46}\text{Sb}_{1.54}\text{Te}_3 + \text{CdTe}$ ⁴⁹, $\text{Bi}_{0.46}\text{Sb}_{1.54}\text{Te}_3 + \text{SnTe}$ ⁵⁰, $\text{Bi}_{0.46}\text{Sb}_{1.54}\text{Te}_3 + \text{SiC}$ ⁵¹, and $\text{Bi}_{0.4}\text{Sb}_{1.6}\text{Te}_3 + \text{CuGaTe}_2$ ⁵².

CONCLUSIONS

A series of $\text{Bi}_{0.5}\text{Sb}_{1.5}\text{Te}_{3+0.3}$ samples with varying concentrations of CrSb magnetic secondary phase (0, 0.125, 0.5, and 1 wt.%) were synthesized by a combination of ball milling and spark plasma sintering techniques. The results showed that the incorporation of small amounts of the CrSb magnetic phase significantly enhanced the thermopower of the samples by in-

creasing the carriers' effective mass, which is consistent with previous findings for magnetic dopants. However, the electrical conductivity is adversely affected by the reduced carrier mobility caused by the presence of the secondary phase. The increased in the power factor, combined with the significantly lower thermal conductivity resulted in a high figure of merit (zT) values for CrSb added samples. These results confirm the potential benefits of incorporating magnetic secondary phases into thermoelectric materials to modulate their electronic and thermal transport properties favorably.

AUTHOR DECLARATIONS

Data availability

The authors declare that the data supporting the findings of this study are available within the paper. Should any raw data files be needed in another format they are available from the corresponding author upon reasonable request.

Declaration of competing interest

The authors have no conflicts to disclose.

ACKNOWLEDGMENTS

This study was supported by the European Union's Horizon 2020 research and innovation program under the Marie Skłodowska-Curie

Grant Agreement No. 801604. This work also received support from the Henry Royce Institute for Advanced Materials, funded through EPSRC grants EP/R00661X/1, EP/S019367/1, EP/P025021/1, and EP/P025498/1. TM would like to thank JST Mirai Program Grant Number JPMJMI19A1. IS was supported by JST SPRING, Grant Number JPMJSP2124.

Appendix A: Heat capacity measurements

The heat capacity of $\text{Bi}_{0.5}\text{Sb}_{1.5}\text{Te}_{3+0.3}$ is displayed in Fig. 5.

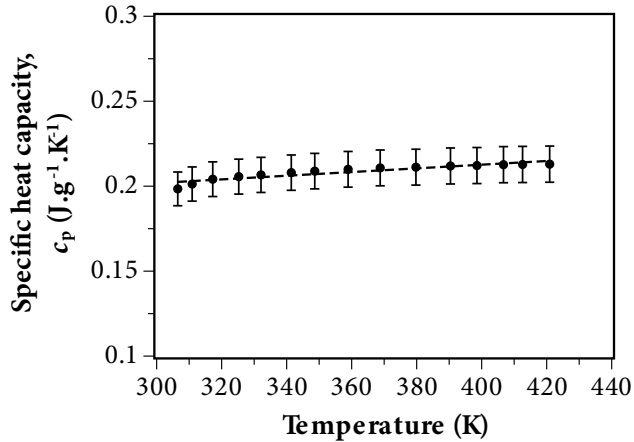


FIG. 5. Temperature-dependent specific heat capacity of $\text{Bi}_{0.5}\text{Sb}_{1.5}\text{Te}_{3+0.3}$. The dashed line represents a linear fit of the data.

Appendix B: Single parabolic band model

For the single parabolic band (SPB) model with acoustic phonons as the main scattering mechanisms, the thermopower, carrier concen-

tration, and Lorenz number are evaluated as

$$\alpha = \pm \frac{k_B}{e} \left(\frac{2F_1(\eta)}{F_0(\eta)} - \eta \right), \quad (\text{B1a})$$

$$n = \frac{(2m^*k_B T)^{3/2}}{2\pi^2\hbar^3} F_{1/2}(\eta), \quad (\text{B1b})$$

$$L = \left(\frac{k_B}{e} \right)^2 \frac{3F_0(\eta)F_2(\eta) - 4F_1(\eta)^2}{F_0(\eta)^2}, \quad (\text{B1c})$$

where e is the elementary charge, k_B is the Boltzmann constant, $\varepsilon = \frac{E}{k_B T}$ is the reduced energy, $\eta = \frac{E_F}{k_B T}$ is the reduced Fermi level, \hbar is the reduced Planck constant, m^* is the density of states effective mass.

$F_j(\eta)$ is the Fermi-Dirac integral for an index j and is defined as

$$F_j(\eta) := \int_0^\infty \frac{\varepsilon^j}{\exp(\varepsilon - \eta) + 1} d\varepsilon. \quad (\text{B2})$$

Since Eq. (B1a) is independent of Eq. (B1b), the procedure for estimating the effective mass was to first calculate the reduced Fermi level from the thermopower measurement and then estimate m^* from the measured carrier concentration.

REFERENCES

- ¹M. Zhang, W. Liu, C. Zhang, S. Xie, Z. Li, F. Hua, J. Luo, Z. Wang, W. Wang, F. Yan, Y. Cao, Y. Liu, Z. Wang, C. Uher, and X. Tang, *ACS Nano* **15**, 5706 (2021).
- ²G. Yang, R. Niu, L. Sang, X. Liao, D. R. G. Mitchell, N. Ye, J. Pei, J.-F. Li, and X. Wang, *Adv. Energy Mater.* **10**, 2000757 (2020).
- ³T. Hendricks, T. Caillat, and T. Mori, *Energies* **15**, 7307 (2022).

- ⁴I. T. Witting, T. C. Chasapis, F. Ricci, M. Peters, N. A. Heinz, G. Hautier, and G. J. Snyder, *Adv. Electron. Mater.* **5**, 10.1002/aelm.201800904 (2019).
- ⁵I. T. Witting, F. Ricci, T. C. Chasapis, G. Hautier, and G. J. Snyder, *Research* **2020**, 1 (2020).
- ⁶F. Ahmed, N. Tsujii, and T. Mori, *J. Mater. Chem.A* **5**, 7545 (2017).
- ⁷W. Koshibae, K. Tsutsui, and S. Maekawa, *Phys. Rev. B* **62**, 6869 (2000).
- ⁸N. Tsujii, A. Nishide, J. Hayakawa, and T. Mori, *Sci. Adv.* **5**, eaat5935 (2019).
- ⁹Y. Zheng, T. Lu, M. M. H. Polash, M. Rasoulianboroujeni, N. Liu, M. E. Manley, Y. Deng, P. J. Sun, X. L. Chen, R. P. Hermann, D. Vashae, J. P. Heremans, and H. Zhao, *Sci. Adv.* **5**, eaat9461 (2019).
- ¹⁰M. Bailyn, *Phys. Rev.* **126**, 2040 (1962).
- ¹¹J. D. Wasscher and C. Haas, *Phys. Lett. B* **8**, 302 (1964).
- ¹²N. Tsujii and T. Mori, *Appl. Phys. Express* **6**, 043001 (2013).
- ¹³R. Ang, A. U. Khan, N. Tsujii, K. Takai, R. Nakamura, and T. Mori, *Angew. Chem. Int. Ed. Engl.* **54**, 12909 (2015), pubmed:26332260.
- ¹⁴C. Peng, G. Zhang, C. Wang, Y. Yan, H. Zheng, Y. Wang, and M. Hu, *physica status solidi (RRL) - Rapid Research Letters* **12**, 1800172 (2018).
- ¹⁵J. B. Vaney, S. A. Yamini, H. Takaki, K. Kobayashi, N. Kobayashi, and T. Mori, *Mater. Today Phys.* **9**, 100090 (2019).
- ¹⁶S. Acharya, S. Anwar, T. Mori, and A. Soni, *J. Mater. Chem. C* **6**, 6489 (2018).
- ¹⁷S. Das, S. M. Valiyaveetil, K.-H. Chen, S. Suwas, and R. C. Mallik, *Mater. Res. Express* **6**, 10.1088/2053-1591/aaf710 (2019).
- ¹⁸H. Matsuura, M. Ogata, T. Mori, and E. Bauer, *Phys. Rev. B* **104**, 214421 (2021).
- ¹⁹W. Zhao, Z. Liu, P. Wei, Q. Zhang, W. Zhu, X. Su, X. Tang, J. Yang, Y. Liu, J. Shi, Y. Chao, S. Lin, and Y. Pei, *Nat. Nanotechnol.* **12**, 55 (2017), pubmed:27723733.
- ²⁰R. Lu, J. S. Lopez, Y. Liu, T. P. Bailey, A. A. Page, S. Wang, C. Uher, and P. F. P. Poudeu, *J. Mater. Chem.A* **7**, 11095 (2019).
- ²¹K. G. Liu and J. Li, *Frontiers of Green Building, Materials and Civil Engineering, Pts 1-8* **71-78**, 3741 (2011).
- ²²C. Bourgès, W. Zhang, K. K. Raut, Y. Owada, N. Kawamoto, M. Mitome, K. Kobayashi, J.-F. c. Halet, D. Berthebaud, and T. Mori, *ACS Appl. Energy Mater.* **6**, 9646 (2023).
- ²³Y.-H. Gao, H. Chen, N. Liu, and R.-Z. Zhang, *Results Phys.* **11**, 915 (2018).
- ²⁴Z. Liu, J. Zhu, P. Wei, W. Zhu, W. Zhao, A. Xia, D. Xu, Y. Lei, and J. Yu, *ACS Appl. Mater. Interfaces* **11**, 45875 (2019).
- ²⁵V. Marghussian, in *Nano-Glass Ceramics* (Elsevier, 2015) pp. 181–223.
- ²⁶G. Tan, F. Shi, S. Hao, H. Chi, T. P. Bailey, L. D. Zhao, C. Uher, C. Wolverton, V. P. Dravid, and M. G. Kanatzidis, *J. Am. Chem. Soc.* **137**, 11507 (2015), pubmed:26308902.
- ²⁷S. Vandendriessche, W. Brullot, D. Slavov, V. K. Valev, and T. Verbiest, *Appl. Phys. Lett.* **102**, 161903 (2013).
- ²⁸W. Zhao, Z. Liu, Z. Sun, Q. Zhang, P. Wei, X. Mu,

- H. Zhou, C. Li, S. Ma, D. He, P. Ji, W. Zhu, X. Nie, X. Su, X. Tang, B. Shen, X. Dong, J. Yang, Y. Liu, and J. Shi, *Nature* **549**, 247 (2017), pubmed:28905895.
- ²⁹H.-L. Zhuang, J. Pei, B. Cai, J. Dong, H. Hu, F.-H. Sun, Y. Pan, G. J. Snyder, and J.-F. Li, *Adv. Funct. Mater.* **31**, 2009681 (2021).
- ³⁰Y. Liu, Y. Zhang, S. Ortega, M. Ibáñez, K. H. Lim, A. Grau-Carbonell, S. Martí-Sánchez, K. M. Ng, J. Arbiol, M. V. Kovalenko, D. Cadavid, and A. Cabot, *Nano Lett.* **18**, 2557 (2018).
- ³¹R. Deng, X. Su, Z. Zheng, W. Liu, Y. Yan, Q. Zhang, V. P. Dravid, C. Uher, M. G. Kanatzidis, and X. Tang, *Sci. Adv.* **4**, eaar5606 (2018).
- ³²N. S. Chauhan, S. V. Pyrlin, O. I. Lebedev, L. S. A. Marques, M. M. D. Ramos, T. Maiti, K. Kovnir, B. A. Korgel, and Y. V. Kolen'ko, *The Journal of Physical Chemistry C* **125**, 20184 (2021).
- ³³H.-S. Kim, N. A. Heinz, Z. M. Gibbs, Y. Tang, S. D. Kang, and G. J. Snyder, *Mater. Today* **20**, 452 (2017).
- ³⁴H. Dohnomae, K. Shintaku, N. Nakayama, and T. Shinjo, *Journal of Magnetism and Magnetic Materials* **126**, 346 (1993).
- ³⁵A. Kanatzia, C. Papageorgiou, C. Lioutas, and T. Kyratsi, *J. Electronic Mater.* **42**, 1652 (2012).
- ³⁶A. International, ASTM E1269-11 10.1520/E1269-11R18 (2018).
- ³⁷M. M. H. Polash, F. Mohaddes, M. Rasoulianboroujeni, and D. Vashae, *J. Mater. Chem. C* **8**, 4049 (2020).
- ³⁸D. K. Ko, Y. Kang, and C. B. Murray, *Nano Lett.* **11**, 2841 (2011), pubmed:21630679.
- ³⁹Y.-X. Zhang, Y.-K. Zhu, D.-S. Song, J. Feng, and Z.-H. Ge, *Chem. Commun.* **57**, 2555 (2021).
- ⁴⁰G. J. Snyder and E. S. Toberer, *Nat. Mater.* **7**, 105 (2008).
- ⁴¹Y. Zheng, Q. Zhang, X. Su, H. Xie, S. Shu, T. Chen, G. Tan, Y. Yan, X. Tang, C. Uher, and G. J. Snyder, *Adv. Energy Mater.* **5**, 1401391 (2015).
- ⁴²R. Fortulan, S. A. Yamini, C. Nwanebu, S. Li, T. Baba, M. J. Reece, and T. Mori, *ACS Applied Energy Materials* **5**, 3845 (2022).
- ⁴³M. Jonson and G. D. Mahan, *Phys. Rev. B* **21**, 4223 (1980).
- ⁴⁴T. Parashchuk, R. Knura, O. Cherniushok, and K. T. Wojciechowski, *ACS Appl. Mater. Interfaces* **14**, 33567 (2022).
- ⁴⁵Z. Wei, C. Wang, L. You, S. Zhao, K. Yang, H. Chen, J. Luo, and X. Chen, *RSC Adv.* **7**, 41111 (2017).
- ⁴⁶S. Bano, D. K. Misra, J. S. Tawale, and S. Auluck, *Journal of Materiomics* **7**, 1264 (2021).
- ⁴⁷C. Li, S. Ma, P. Wei, W. Zhu, X. Nie, X. Sang, Z. Sun, Q. Zhang, and W. Zhao, *Energ. Environ. Sci.* **13**, 535 (2020).
- ⁴⁸G. Yang, L. Sang, F. F. Yun, D. R. G. Mitchell, G. Casillas, N. Ye, K. See, J. Pei, X. Wang, J.-F. Li, G. J. Snyder, and X. Wang, *Adv. Funct. Mater.* **31**, 2008851 (2021).
- ⁴⁹Q. Tao, R. Deng, J. Li, Y. Yan, X. Su, P. F. P. Poudeu, and X. Tang, *ACS Appl. Mater. Interfaces* **12**, 26330 (2020).
- ⁵⁰D. Zhang, J. Wang, L. Zhang, J. Lei, Z. Ma, C. Wang, W. Guan, Z. Cheng, and Y. Wang, *ACS Appl. Mater. Interfaces* **11**, 36658 (2019).
- ⁵¹D. Zhang, J. Lei, W. Guan, Z. Ma, C. Wang, L. Zhang, Z. Cheng, and Y. Wang, *J. Alloys Compd.* **784**, 1276

(2019).

172, 88 (2019).

⁵²Y. Li, X. Wang, G. Liu, B. Shin, and F. Shan, *Scr. Mater.*